

## DISCOVERY OF SPATIAL PERIODICITIES IN A CORONAL LOOP USING AUTOMATED EDGE-TRACKING ALGORITHMS

D. B. JESS

School of Mathematics and Physics, Astrophysics Research Centre, Queen's University, Belfast BT7 1NN, Northern Ireland, UK;  
and Solar Physics Laboratory, NASA Goddard Space Flight Center, Code 671, Greenbelt, MD 20771; djess01@qub.ac.uk

M. MATHIOUDAKIS

School of Mathematics and Physics, Astrophysics Research Centre, Queen's University, Belfast BT7 1NN, Northern Ireland, UK

R. ERDÉLYI AND G. VERTH

SP<sup>2</sup>RC, Department of Applied Mathematics, University of Sheffield, Sheffield S3 7RH, England, UK

R. T. J. McAULIFFE

Solar Physics Laboratory, NASA Goddard Space Flight Center, Code 671, Greenbelt, MD 20771; and Catholic University of America,  
620 Michigan Avenue NE, Washington, DC 20064

AND

F. P. KEENAN

School of Mathematics and Physics, Astrophysics Research Centre, Queen's University, Belfast BT7 1NN, Northern Ireland, UK

Received 2007 November 5; accepted 2008 February 13

### ABSTRACT

A new method for automated coronal loop tracking, in both spatial and temporal domains, is presented. Applying this technique to *TRACE* data, obtained using the 171 Å filter on 1998 July 14, we detect a coronal loop undergoing a 270 s kink-mode oscillation, as previously found by Aschwanden et al. However, we also detect flare-induced, and previously unnoticed, *spatial periodicities* on a scale of 3500 km, which occur along the coronal loop edge. Furthermore, we establish a reduction in oscillatory power for these spatial periodicities of 45% over a 222 s interval. We relate the reduction in detected oscillatory power to the physical damping of these loop-top oscillations.

*Subject headings:* methods: data analysis — Sun: corona — Sun: evolution — Sun: oscillations —  
techniques: image processing

*Online material:* color figures

### 1. INTRODUCTION

Automated feature recognition and tracking has long been a goal for scientists. With the advent of higher sensitivity satellite-based telescopes and the resulting increase in readout rates, it is imperative to be able to do some preliminary data analysis in real time. Without this ability, the large data rates achievable make it extremely difficult to implement onboard trigger programs (e.g., a flare trigger) that allow the telescope pointing to be redirected to an area of interest almost immediately. Furthermore, having a means of establishing solar phenomena in real time allows instrument users to select data sets of particular interest much more readily than in the past. Thus, many schemes have been set up to push this form of real-time data analysis forward, including the Heliophysics Knowledge Base program, which will enable real-time detections of oscillatory phenomena occurring on the Sun.

Current satellites, in particular the *Transition Region and Coronal Explorer* (*TRACE*), have enabled the analysis of many oscillatory signatures originating within the outer solar atmosphere. Aschwanden et al. (1999), Schrijver et al. (2002), Wang & Solanki (2004), De Pontieu et al. (2005), and Marsh & Walsh (2006), just to name a few typical examples (a recent review is in, e.g., Banerjee et al. 2007), all report oscillatory phenomena occurring within coronal loop structures. Previously, however, the majority of work on oscillating coronal loops has been focused on the temporal domain (e.g., Nakariakov et al. 1999). However, it was suggested by Erdélyi & Verth (2007) and Verth et al. (2007) that the imaging capacities of current and future high-resolution instru-

ments should allow us to investigate oscillatory phenomena in the spatial domain (e.g., along the observed waveguide). Inspired by these suggestions, in this work we investigate the spatial evolution of a coronal loop structure, independent of its position during a flare-induced kink oscillation. From this we can understand the behavior of the loop in the spatial domain and analyze any phenomena that are flare induced, yet confined to the volume occupied by the loop. In § 2 we describe the observations, while in § 3 we discuss the methodologies used during the analysis of the data which allow us to accurately track the spatial evolution of coronal loops. A discussion of our results in the context of confined loop oscillations is given in § 4, and our concluding remarks are in § 5.

### 2. OBSERVATIONS

The data presented here are part of an observing sequence obtained on 1998 July 14, using the *TRACE* imaging satellite. The optical setup of *TRACE* allowed a 384'' × 384'' area surrounding active region NOAA 8270 to be investigated with a spatial sampling of 0.5'' pixel<sup>-1</sup>. The 171 Å filter was selected for these observations, which has an inherent passband width of 6.4 Å, allowing plasma in the temperature range 0.2–2.0 MK to be studied. The cadence of the *TRACE* instrument was not constant during the observing sequence, with the time between successive exposures varying between 66 and 82 s.

Our data set consists of 88 successive *TRACE* images providing nearly 2 hr of continuous, uninterrupted data. During the observing

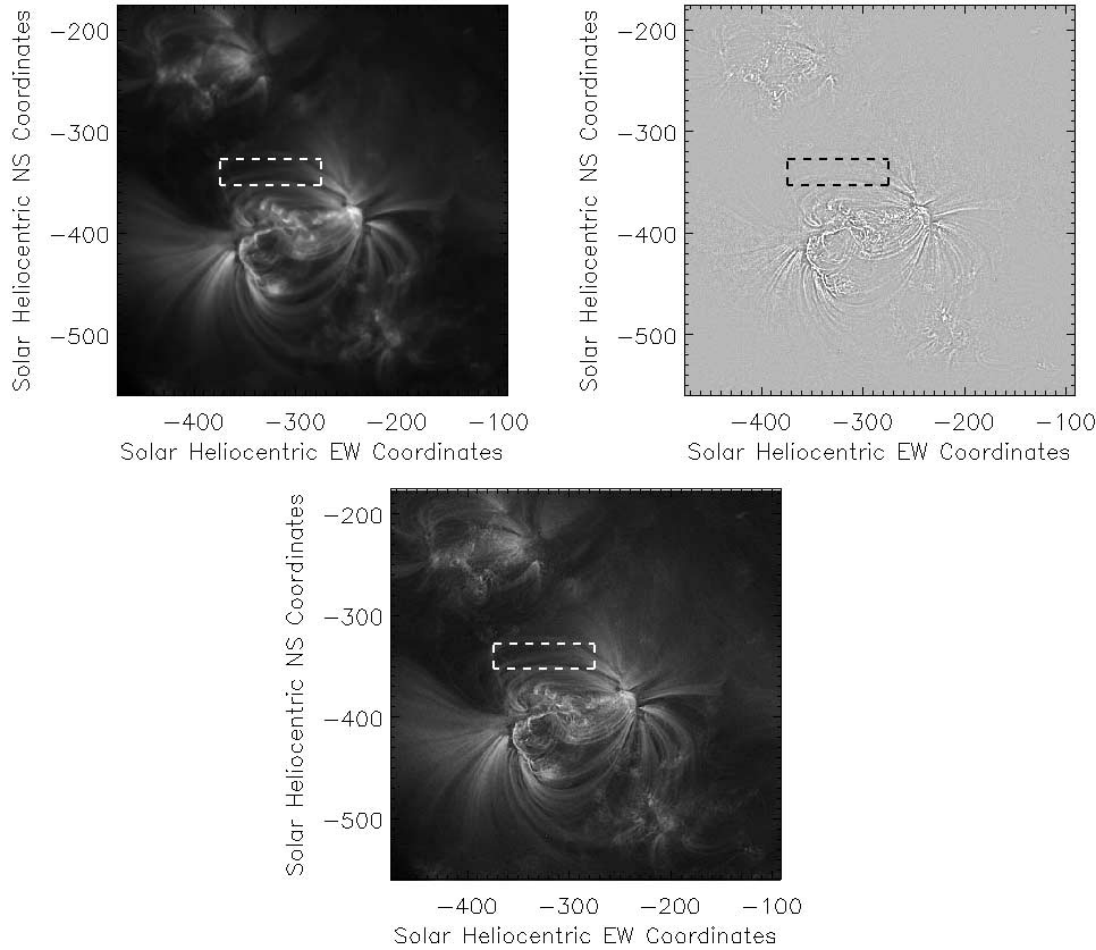


FIG. 1.—Complete *TRACE* field of view (top left) after undergoing initial processing using the *trace\_prep.pro* IDL routine. The top right image shows the fine-scale structures detected using the Laplacian filter outlined in § 3.1, and the bottom image reveals the sharpened *TRACE* field of view after the addition of fine-scale structures. Note how the clarity of loop structures is drastically increased. Overplotted dashed lines in each image outline the region of interest selected for this paper.

sequence, a large M4.6 flare occurred in the immediate vicinity of the active region under investigation.

### 3. DATA ANALYSIS

The *TRACE* data were retrieved directly from the Lockheed Martin Solar and Astrophysics Labs database and were subjected to standard processing algorithms: The IDL routine *trace\_prep.pro* was implemented to remove cosmic-ray streaks, reduce readout noise, and prepare the data in a user-friendly format. Derotation of the *TRACE* images was also deemed necessary, since the observing sequence lasts approximately 2 hr, equating to a relatively large solar rotation (20" at disk center). From this point, it was possible to use additional programs to aid in the analysis of the data as described in detail below.

#### 3.1. Laplacian Image Sharpening

We implement a form of Laplacian image sharpening. Using the same  $3 \times 3$  convolution kernel implemented by Gonzalez & Woods (1992) we are able to enhance the fine-scale structure found in the *TRACE* images. Figure 1 shows the result of applying the convolution kernel to a full *TRACE* image. Note the amount of fine detail found in this filtered image (top right panel of Fig. 1). The next step is to add this fine-scale information back into the original image in order to sharpen the image. Note, in the bottom panel of Figure 1, the emphasis of fine structures when compared to the original, unfiltered image. Figure 1 demonstrates

that these processes are readily applicable to full-size *TRACE* fields of view due to the fast processing ability of modern-day computers. For the purposes of the data under investigation here, all *TRACE* images were subjected to Laplacian image-sharpening routines.

#### 3.2. Wavelet Modulus Maxima Edge Detection

After successful completion of image sharpening, edge detection algorithms can be implemented. The sharpened images have increased fine-scale information and as such provide the necessary platform for establishing feature edges that may have been previously unresolvable. Immediately after the flare event, one particular coronal loop is seen to oscillate. This kink-mode oscillation has been investigated many times (see Aschwanden et al. 1999 for the initial investigation) in the temporal domain. However, following Erdélyi & Verth (2007) we propose here to investigate the behavior of the loop in the spatial domain. In order to track the spatial behavior of the loop, an automated routine was devised to minimize errors introduced through human interaction with the data.

The first step involves intensity thresholding, whereby features in the *TRACE* field of view are contoured depending on their emissive flux. Threshold limits for contouring are entirely arbitrary and as such may vary from data set to data set, as well as for which features are desirable to contour. However, for the data presented here, a lower intensity threshold of the background

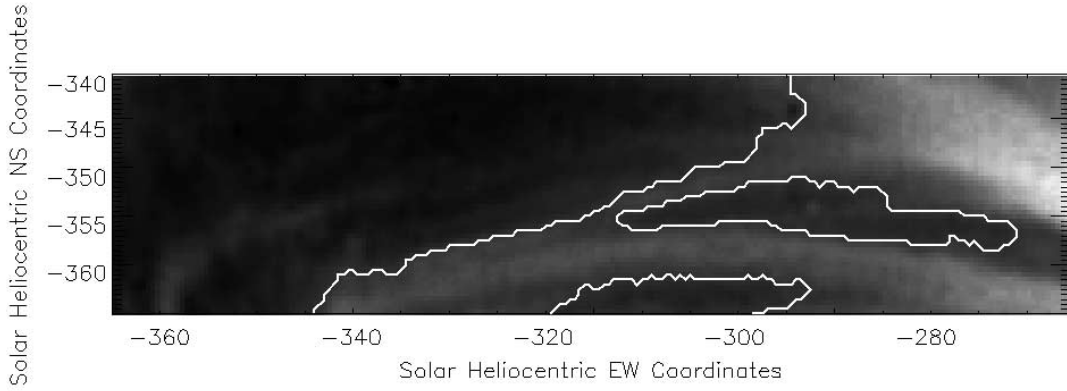


FIG. 2.—Contoured (*bold white line*) *TRACE* coronal loop using a minimum intensity threshold of the background median value plus  $5\sigma$ . From this threshold value we can see that the loop is contoured accurately with minimal solar background included.

median value plus  $5\sigma$  is used. This value allowed us to contour *TRACE* coronal loop structures, yet leave out background quiet Sun as shown in Figure 2. To emphasize feature edges and remove shallow intensity gradients, a binary format for feature mapping is used. All pixels that lie above the lower intensity threshold defined above are assigned a value of “1.” Those pixels that lie below the threshold were assigned a value of “0,” as seen in Figure 3. This binary format provides an absolute intensity cutoff, thus providing a definite feature edge that can be tracked, both spatially and temporally. Placing the images into binary format was deemed necessary due to the poor spatial resolution of the *TRACE* spacecraft, whereby neighboring bright features are hard to distinguish unless a form of thresholding is used. Future instruments, which provide higher spatial resolution, should eradicate the need for binary formatting. The binary image is padded using a zeroed array from which feature edge tracking can commence.

Tracking of this feature edge is performed using a wavelet modulus maxima (WMM) technique (Muzy et al. 1993; McAteer et al. 2007). From the padded binary array created above, a horizontal pixel is chosen. Figure 4 shows the selection of horizontal pixel 125, as indicated by the vertical dashed line, as well as the corresponding intensity plot along this vertical line. A wavelet transform is produced for this intensity plot, demonstrated in Figure 4, utilizing a Mexican hat wavelet. A Mexican hat wavelet, which is a double derivative of the traditional Morlet wavelet, is very useful for detecting sharp intensity gradients that are present due to the binary format implemented above. An absolute wavelet power spectrum is plotted as a function of vertical

pixel element in Figure 5. In addition, maximum wavelet power features are traced down to the  $x$ -axis of the power spectrum and reveal the locations of maximum intensity gradients. Figure 5 replots the intensity in the vertical direction at horizontal pixel 125, and it can be seen that where the maximum wavelet power meets the  $x$ -axis also corresponds to the edges of the *TRACE* coronal loop under investigation.

From Figure 2, it is clear that better contrast is achieved at the northern edge of the loop, where its brightness overlies fainter, less intense, quiet Sun. By contrast, the southern edge of the loop in Figure 2 is difficult to separate from other loop structures, due to the densely packed nature of such features closer to active regions. Since in this instance it is desirable to track the upper edge of the coronal loop, we disregard the first maximum wavelet power location and record the position where the second maximum wavelet power location intersects with the  $x$ -axis. This pinpoints the exact location of the northerly edge of the coronal loop in question. This process is repeated over the entire east-west direction and for all frames in the observing sequence, with the subsequent position of the northern edge of the *TRACE* coronal loop recorded. From the resulting loop edge positions it is possible to analyze both temporal and spatial variations.

#### 4. RESULTS AND DISCUSSION

Our main goal is to investigate the spatial behavior of the oscillating coronal loop. However, to verify that the presented loop-tracking routine is functioning properly, derived results in the temporal domain are compared to previous findings. To compensate

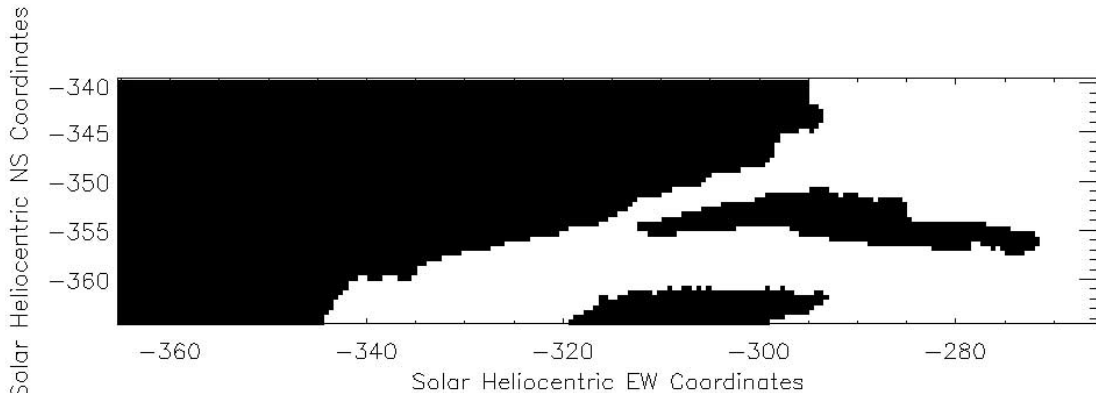


FIG. 3.—Contours obtained in Fig. 2 converted to a binary scale as defined in § 3.2. This provides the sharp intensity gradient required for accurate feature edge detection and tracking.

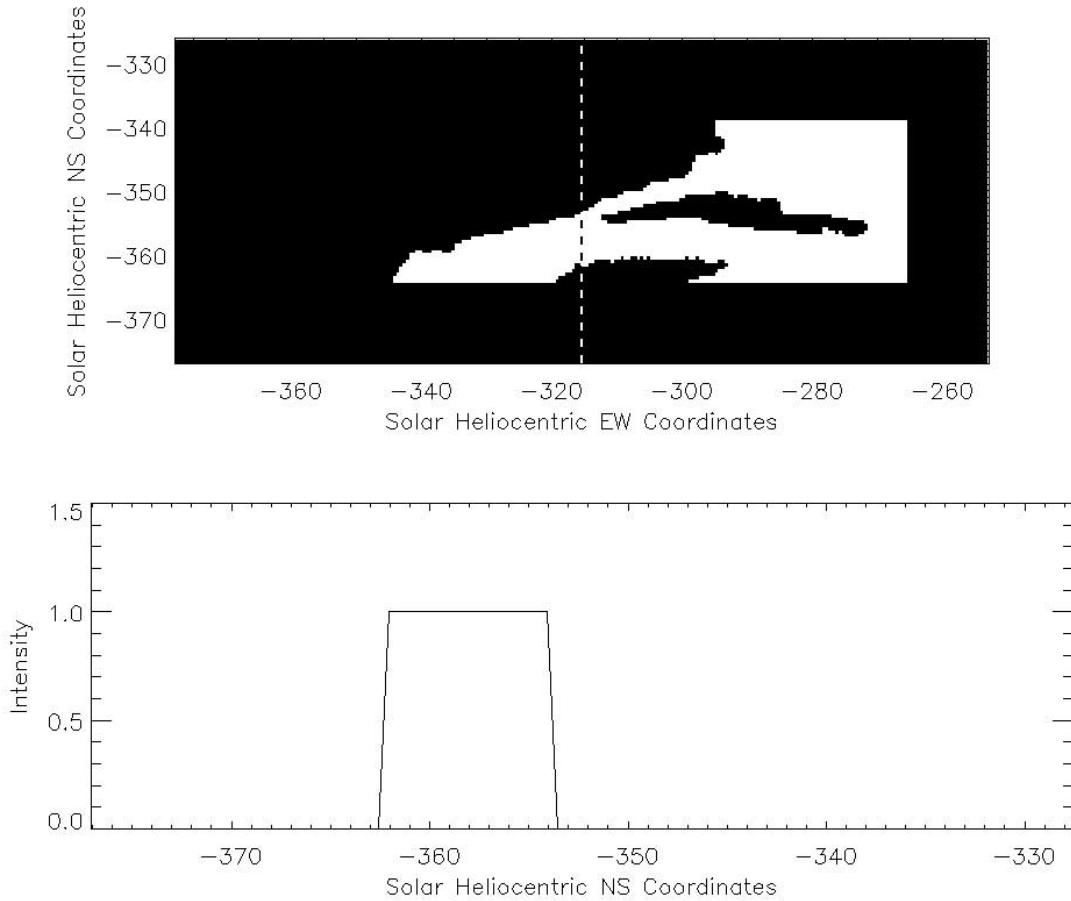


Fig. 4.—Upper panel shows the binary-formatted image obtained in Fig. 3 inserted into a padded, zeroed array that provides the best platform for WMM edge detection. A vertical dashed line at  $x$  pixel 125, corresponding to a heliocentric east-west coordinate of  $-315''$ , is drawn, with the resulting intensity plot, along the north-south direction for this  $x$  pixel, shown in the bottom panel.

for the timing irregularity outlined in § 2, all data were interpolated onto a constant-cadence time series with linear interpolation performed between data points. This provides the necessary platform for temporal studies to commence. Maintaining consistency with the previous example, a plot indicating the variation with time of the location of the northern edge of the coronal loop, for horizontal pixel 125, is displayed in Figure 6. It is clear that a periodicity of approximately 270 s exists, consistent with the findings of Aschwanden et al. (1999). This result implies that the loop detection and tracking algorithms, developed here, are functioning accurately.

From Figure 6, it appears that the oscillating coronal loop passes through an equilibrium position at times of 0, 280, and 502 s, with the overall shape of the loop similar at the corresponding *TRACE* frames. If indeed the shape of the loop is identical at times of 0, 280, and 502 s, then a subtraction of any two of these loop shapes should provide a resulting image equal to zero. However, on subtraction of the loop shape at 0 s from that at 280 s, a spatial periodicity is revealed. Running this resulting loop shape through a one-dimensional spatial wavelet transform establishes an oscillatory period along the northern loop edge of 10 pixels (Fig. 7). A number of strict criteria implemented on the data, including the test against spurious detections of power that may be due to Poisson noise, the comparison of the input light curve with a large number (1500) of randomized time series with an identical distribution of counts (see O’Shea et al. 2001 for a detailed explanation), and the exclusion of oscillations that last, in du-

ration, less than 1.41 cycles, allowed us to ensure that oscillatory signatures correspond to real periodicities. These criteria have been described in detail in previous papers (see Jess et al. 2007; Banerjee et al. 2001; McAteer et al. 2004; Ireland et al. 1999; Mathioudakis et al. 2003). Furthermore, according to the Ritz theorem of variational principles (Ritz 1908), spatial amplitude dependence is much more sensitive to structural changes of the magnetic loop (e.g., stratification, magnetic field divergence, twist, etc.) than the traditionally studied period ratios of FFT-identified modes of oscillations. Thus, analyzing spatial variations, rather than the more traditional temporal variations, will provide a useful platform on which to maximize the limited resolution of current satellite imagers. For the *TRACE* plate scale equal to  $0.5''$  pixel $^{-1}$ , the detected 10 pixel periodicity corresponds to an absolute spatial distance, or wavelength, of approximately 3500 km per complete oscillation (more than three complete cycles detected).

To investigate if this periodicity is visible at the following equilibrium position (502 s), we subtract the loop shape at 0 s from that at 502 s, and pass through our one-dimensional spatial wavelet transform. The resulting evidence, shown in Figure 8, indicates that the 10 pixel spatial periodicity is indeed still present, albeit with a reduction in oscillatory power. We interpret the reduction in oscillatory power as the physical signature of damping of the loop-top oscillations. On further inspection of Figures 7 and 8, we see that the oscillatory power, in normalized digital number (DN), has dropped from 29 to 16 over the 222 s interval. This equates to a 45% decrease in oscillatory power and is consistent

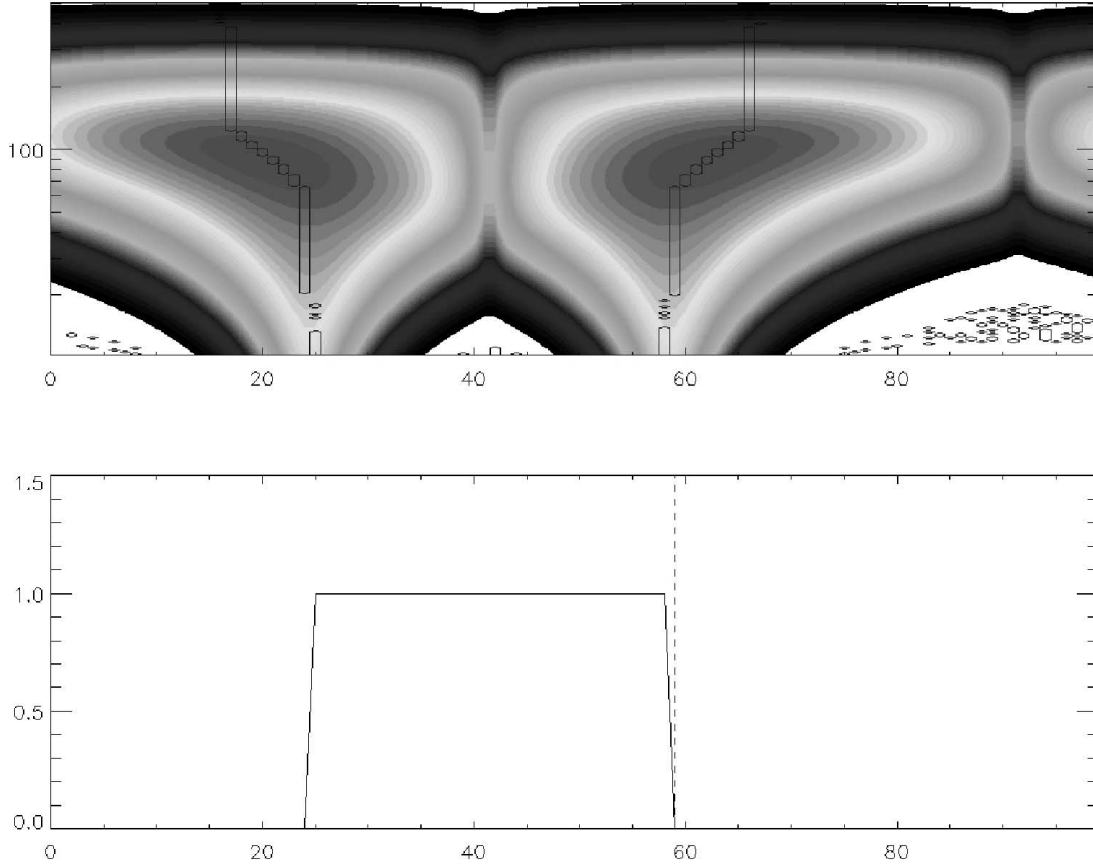


FIG. 5.—One-dimensional spatial wavelet power spectrum (*top*) generated along the vertical spatial direction of the *TRACE* field of view for horizontal pixel No. 125. This panel also shows regions of maximum power being traced down to the intersect point on the *x*-axis. The intensity plot from Fig. 4 is again plotted (*bottom*) with a dashed line indicating the position of intersection of the maximum wavelet power traces with the *x*-axis. Notice how the *x*-axis intersect position of maximum wavelet power corresponds exactly to the reduction of intensity in the bottom panel. This reduction in intensity is analogous with the upper edge of the *TRACE* coronal loop, showing the accuracy of this method when detecting feature edges. [See the electronic edition of the *Journal* for a color version of this figure.]

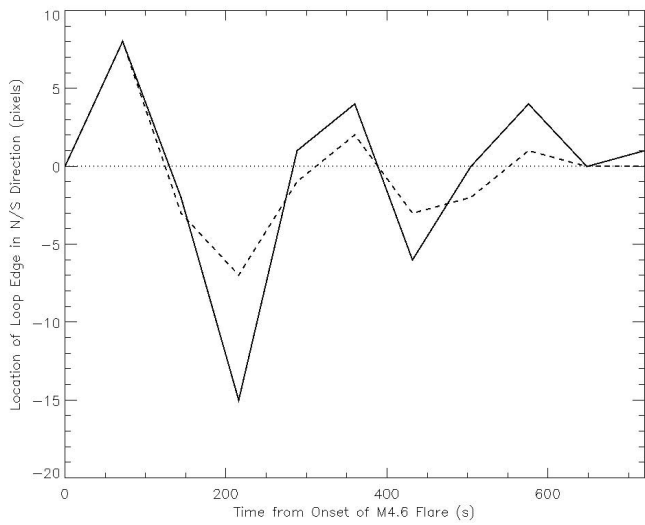


FIG. 6.—Temporal evolution of a particular portion of the oscillating coronal loop. Here, shown as a bold line, we see a periodicity of approximately 270 s related to the kink-mode oscillation of the loop and the subsequent damping of the amplitude with time. The dashed line indicates the temporal periodicity detected when a lower intensity threshold is used to contour the loop edge, while the dotted line indicates the equilibrium position of the loop. A lower intensity threshold (see § 4) reveals the same periodicity, indicating that the loop edge tracking, due to high contrast between the loop and surrounding quiet Sun, is not overly sensitive to threshold values.

with other aspects of coronal loop oscillations, which are seen to be heavily damped (Aschwanden et al. 2003; Ruderman 2005; Terradas et al. 2006; Dymova & Ruderman 2007).

To investigate a possible phase relationship (Athay & White 1978; O’Shea et al. 2007) we create a cross-wavelet power spectrum between the two detected loop-top oscillations and inspect the resulting spatial phase diagram (Fig. 9). This figure reveals a clear phase shift, over many complete wavelengths, of  $0^\circ$  to  $-50^\circ$ . Due to the long kink oscillation period ( $\approx 270$  s) and the relatively poor, and irregular, cadence of the *TRACE* instrument, we are only able to evaluate kink equilibrium spatial periodicities at two times during the presented data set. At these two times, the coronal loop undergoing the kink oscillation has returned to its equilibrium state, i.e., matching the shape and position of the loop prior to the flare-induced kink oscillation. Between these two equilibrium states, the loop in question has undergone one complete kink oscillation cycle.

However, since we cannot evaluate more than two kink equilibrium spatial periodicities, we are unable to determine the direction of wave propagation. Three or more kink equilibrium positions would allow for a comparison of phase differences, thus providing an indication to the direction of wave propagation. Thus, a phase shift of  $0^\circ$  to  $-50^\circ$  may equally be represented as  $(360n)^\circ$  to  $(360n-50)^\circ$ , where  $n$  is an integer number arising from the low sampling rate of the *TRACE* instrument. As described by Athay & White (1979) and O’Shea et al. (2006), the errors associated with the phase shift can only be constrained and determined unambiguously by careful measurements over the full range of

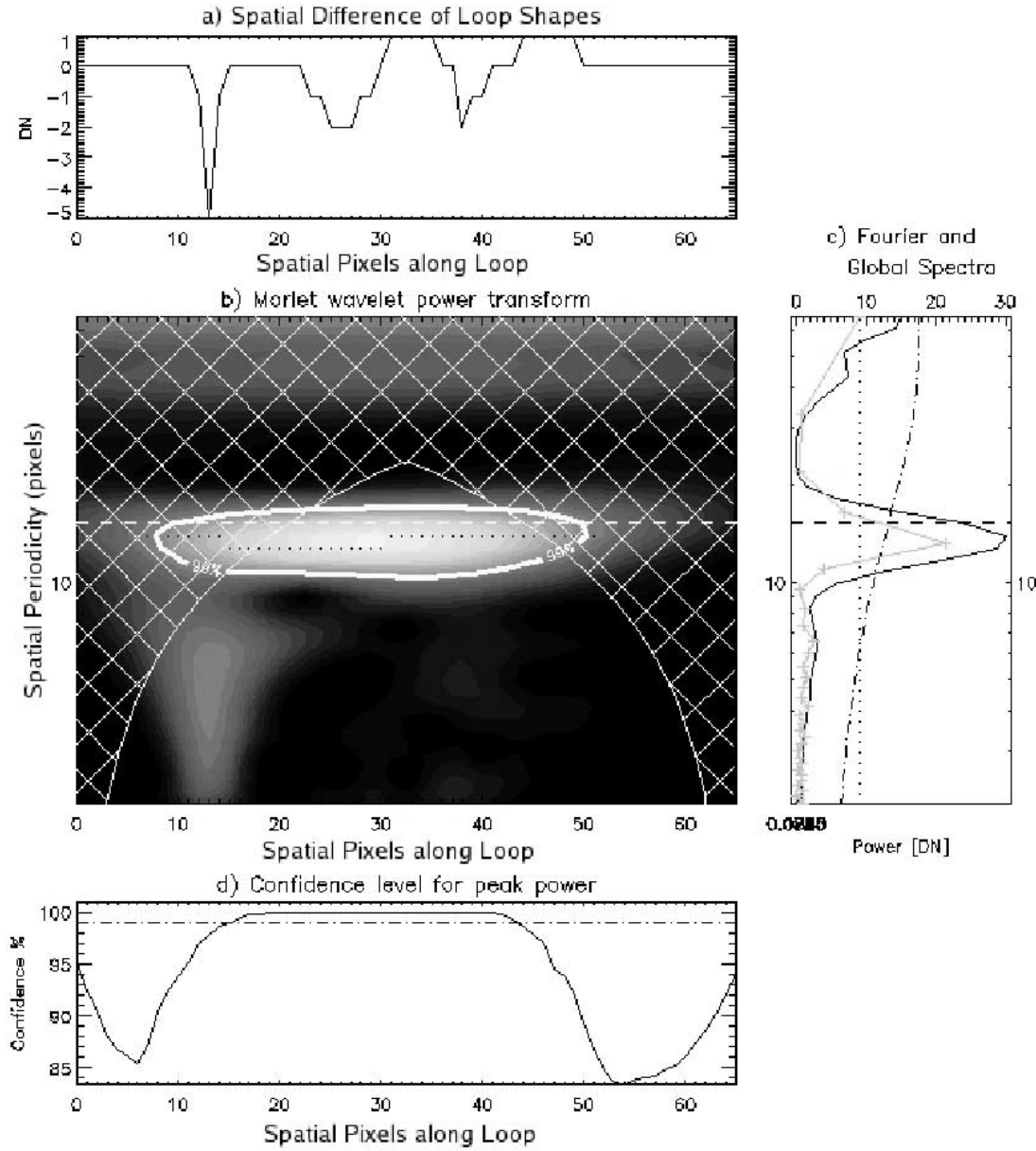


FIG. 7.—Detection of a 10 pixel spatial oscillation. The resulting northern loop edge outline created by the subtraction of the loop edge at 0 s from the loop edge at 280 s after the flare event is shown in (a). The one-dimensional spatial wavelet power transform along with locations where detected power is at, or above, the 99% confidence level are contained within the contours in (b). Plot c shows the summation of the wavelet power transform over time (solid line) and the fast Fourier power spectrum (crosses) over time, plotted as a function of period. Both methods have detected a well-pronounced 10 pixel spatial oscillation. The global wavelet (dash-dotted line) and Fourier (dotted line) 95% significance levels are also plotted. The cone of influence (COI, cross-hatched area in the plot), defines an area in the wavelet diagram where edge effects become important and as such any frequencies outside the COI are disregarded. Periods above the horizontal line (dotted) fall within the COI. The probability levels, which are related to the percentage confidence attributed to the peak power at every time step in the wavelet transform, are plotted in (d). [See the electronic edition of the Journal for a color version of this figure.]

observed wavelengths. To reduce the errors involved with phase difference analysis we evaluate the phase shift over a number of different wavelengths. Through examination of the Fourier and global spectra associated with the detected 3500 km spatial oscillation, in addition to the boundaries of the 99% confidence level contours, we find that the FWHM of the presented oscillation is 5 pixels, or  $\approx 1800$  km. This corresponds to 42 wavelength resolution elements, when a 0.016 spacing between discrete scales is used, in the evaluation of the cross-wavelet power spectrum (Torrence & Compo 1998). Performing phase difference analysis on each of the 42 wavelength elements, spanning a wavelength coverage of 2600–4400 km, we are able to verify the existence of a  $0^\circ$  to  $-50^\circ$  phase shift. More importantly, we can reduce the

error associated with the calculated phase differences through examination of the multiple wavelength elements. The bottom panel of Figure 9 includes the maximum deviation, from the average spatial phase diagram, induced by the analyses of 42 wavelength resolution elements. It can be seen from Figure 9 that the phase error bars do not detract from the generalized shape of the spatial phase diagram, thus validating the existence of a  $0^\circ$  to  $-50^\circ$  phase shift.

In order to validate our results, we have undertaken a number of further rigorous tests. We have implemented the same loop edge detection and tracking processes on additional coronal loops away from the region under investigation, yet within the same *TRACE* field of view. Since these loops are not connected with

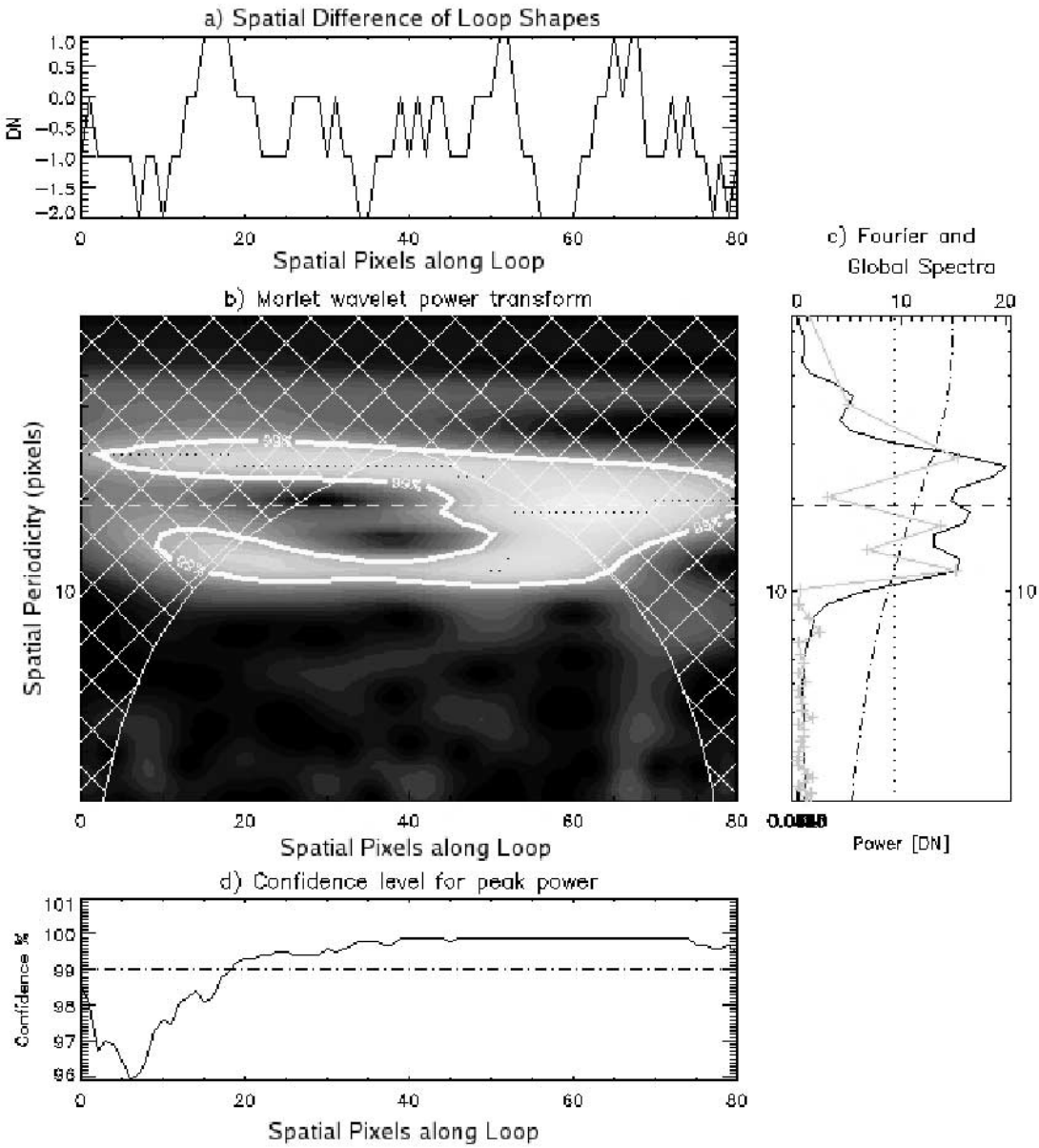


FIG. 8.—Identical plot to Fig. 7, except that the loop edge outline shown in (a) results from the subtraction of the loop edge at 0 s from the loop edge at 502 s after the flare event. We can see that a 10 pixel spatial periodicity is still evident, albeit with a reduction in normalized oscillatory power. [See the electronic edition of the Journal for a color version of this figure.]

the flare event and therefore not seen to oscillate, no spatial periodicities along the loop would be expected when two loop outlines are subtracted from one another. Subtracting the control loop outline at 0 s from that at 280 s after the flare, to remain consistent with the work above, and running through a one-dimensional spatial wavelet transform reveals no periodicities. Furthermore, we tested for spatial periodicities, on the loop seen to oscillate, both prior to, and long after, the flare event. These tests found no oscillatory phenomena in either instance, indicating that the spatial periodicities detected are flare induced. To further test the abilities of the presented algorithm we carry out an identical form of analysis on an additional case of an oscillating coronal loop observed by *TRACE* on 2001 April 15. We chose a loop arcade which is seen to oscillate after being buffeted by a neighboring X14.4 flare originating from NOAA 9415. Implementing our algorithm on this data set we are able to corroborate the kink periodicity and associated decay time described by Verwichte et al. (2004). However, in this instance no coronal loop spatial

periodicities could be found. The presented algorithm is therefore applicable to all data sets and is a reliable tool for detecting kink oscillations.

In addition, to verify that the detected oscillation is not an artifact of the loop-tracking algorithm, we have designed a numerical simulation to test the reliability of our oscillatory signal. A synthetic wave train is generated that is identical in both amplitude and wavelength to the detected *TRACE* oscillations and propagates with an Alfvén speed of  $1000 \text{ km s}^{-1}$  (Nakariakov & Verwichte 2005). A resultant wave, formed from the numerical integration with time, is created based on real exposure times extracted from the *TRACE* image files. As would be expected, if the exposure time is an exact integer multiple of the oscillatory period, the resultant waveform equals zero at all spatial locations (Fig 10). This is due to

$$\int_0^{n2\pi} \sin t dt = 0, \quad (1)$$

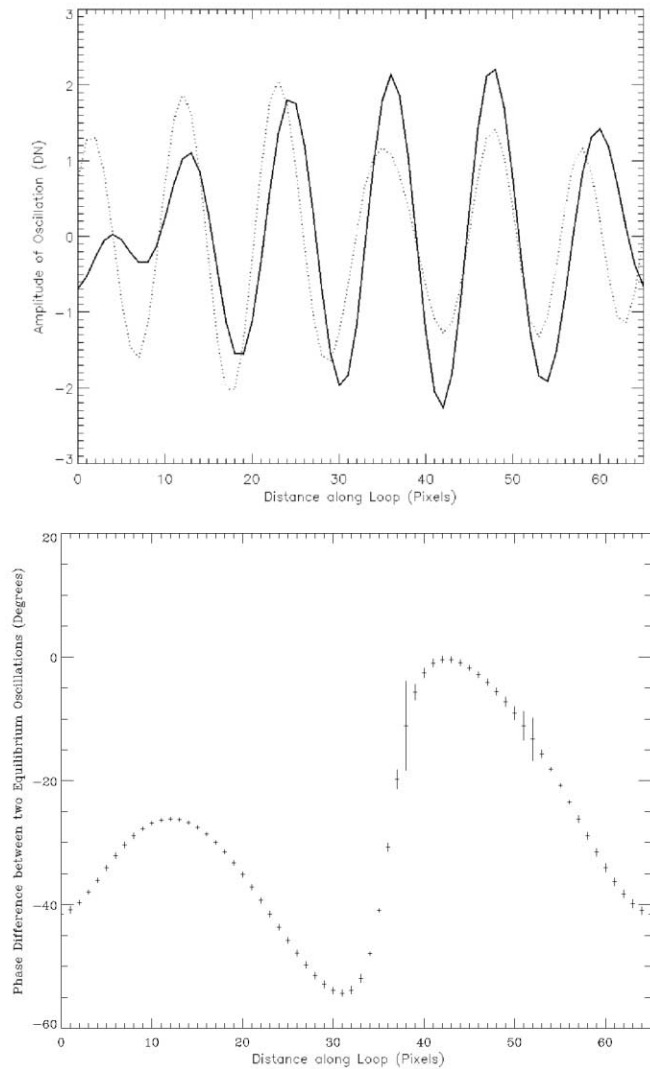


FIG. 9.—Top panel shows the oscillation amplitude as a function of position along the loop for both loop-top oscillations. The solid line relates to the spatial periodicity detected between times of 0 and 280 s, while the dotted line relates to the spatial periodicity detected between times of 0 and 502 s. From this plot, it is clear to see a phase shift between the two loop-top oscillations. The bottom panel shows the phase-difference results of a cross-wavelet spectrum of the two detected spatial oscillations. Maximum phase deviations from the average spatial phase curve, as detailed in § 4, are plotted as vertical error bars. We can clearly see a phase shift, on the order of  $0^\circ$  to  $-50^\circ$ , over the duration of six complete cycles.

where  $n$  is an integer number and  $t$  is time. By contrast, if the exposure time is set to a value *not equal* to an integer multiple of the period, then the propagating wave can be detected. Figure 11 shows the resultant wave, formed using the exact exposure time taken from the *TRACE* images. It is clear, from Figure 11, that even though multiple oscillatory cycles pass through the same pixel on the detector, an oscillatory periodicity can still be detected.

Throughout the analysis of the presented results, we interpret the translation of the coronal loop, in both the temporal *and* spatial domains, to be the result of the physical movement of this feature. Other aspects may accompany, and subsequently aid in, the movement of the loop. Things such as a change in temperature or a change in inclination angle may result in line-of-sight intensity changes. Since the *TRACE* bandpass used allows a wide range of coronal temperatures to be investigated, and since the movement of the loop edge is restricted to  $<10''$ , we feel confident that the

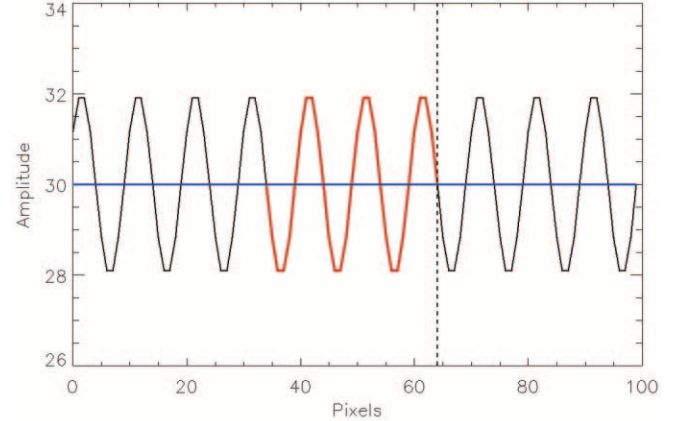


FIG. 10.—Integrated waveform when the exposure time is equal to an integer number of complete periods. The black wave train is a sinusoid, equal in both amplitude and wavelength to the observed *TRACE* spatial oscillation. The bold red line indicates the portion of the input wave train that passes through an arbitrary spatial location, as denoted by the vertical black dashed line, during the exposure time. The result of integrating over the chosen exposure time is plotted as a bold blue line. It is clear that the resultant wave, when the exposure time is equal to an integer multiple of the period, equals zero. This wave will therefore not be detectable by the *TRACE* instrument.

main source of translation is caused by the physical movement of the loop itself.

## 5. CONCLUDING REMARKS

A new method for the detection, and subsequent tracking, of coronal loop structures is presented. This method also provides the ability to simultaneously search for longitudinal and transverse oscillations in real time. It is possible to detect the periodic loop displacement caused by the influence of transverse waves, and in addition the intensity fluctuations, due to density restrictions and rarefactions, synonymous with longitudinal oscillations can also be easily identified through concurrent time-series analysis. Through the subtraction of loop outlines, we are essentially removing general features and shapes that remain constant from frame to frame, yet magnifying features that evolve or change spatial position.

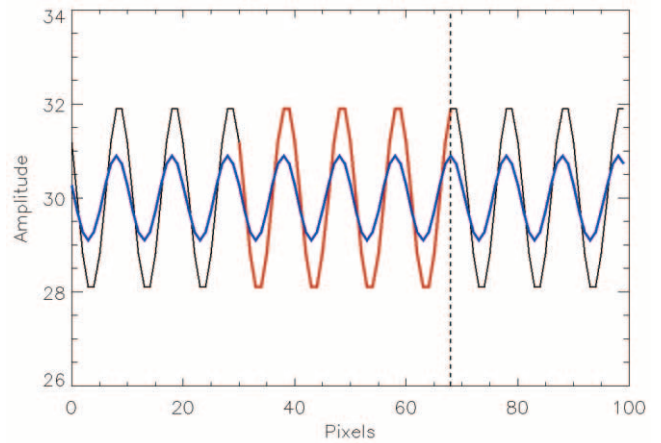


FIG. 11.—Identical plot to Fig. 10, only showing the resultant waveform produced when the exposure time matches that of the *TRACE* instrument. It is clear that the resultant wave, unmodified in wavelength, is still detectable even when multiple oscillations pass through the same pixel on the detector. This plot demonstrates that our detected 3500 km spatial periodicity is real.

Utilizing our method for automated coronal loop analysis, we have detected spatial periodicities, on the scale of 3500 km per cycle, occurring on a coronal loop immediately after being buffeted by a neighboring M4.6 flare. We detect the damping of these loop-top oscillations, with a 45% reduction in oscillatory power over a 222 s interval. In addition, we find a wrapped spatial phase shift of  $0^\circ$  to  $-50^\circ$ , related to the time interval of 222 s between successive kink oscillation equilibrium positions, for the traveling loop-top oscillations.

We propose that the above methodology will be useful in the future, especially with both temporal and spatial resolutions of space-borne solar telescopes constantly improving. From coronal imagers available on the upcoming *Solar Dynamics Observatory* and *Solar Orbiter*, as well as the recently launched *Hinode* satellite, there will be a wealth of high-resolution images containing abundances of coronal loop oscillations. There are a number of currently available methods to detect and analyze such oscillatory phenomena. Such techniques may be data specific and therefore not applicable to a wide range of varying coronal observations. However, our technique is designed to be readily applicable to

all coronal data sets and is a great asset when spatial resolutions are of the highest order due to the WTMM techniques outlined here. We suggest that the currently presented method provides further excellent capabilities for the detection of both temporal and spatial coronal loop oscillations.

D. B. J. is supported by a Northern Ireland Department for Employment and Learning studentship. D. B. J. additionally thanks NASA Goddard Space Flight Center for a CAST studentship—in particular, Doug Rabin and Roger Thomas deserve special thanks for their endless help, support, and scientific input. R. E. acknowledges M. Kéray for patient encouragement and is also grateful to NSF, Hungary (OTKA, Ref. No. K67746). F. P. K. is grateful to A. W. E. Aldermaston for the award of a William Penney Fellowship. Wavelet software was provided by C. Torrence and G. P. Compo.<sup>1</sup>

<sup>1</sup> Wavelet software is available at <http://paos.colorado.edu/research/wavelets/>.

#### REFERENCES

Aschwanden, M. J., Fletcher, L., Schrijver, C. J., & Alexander, D. 1999, *ApJ*, 520, 880  
 Aschwanden, M. J., Nightingale, R. W., Andries, J., Goossens, M., & Van Doorsselaere, T. 2003, *ApJ*, 598, 1375  
 Athay, R. G., & White, O. R. 1978, *ApJ*, 226, 1135  
 ———. 1979, *ApJ*, 229, 1147  
 Banerjee, D., Erdélyi, R., Oliver, R., & O’Shea, E. 2007, *Sol. Phys.*, 246, 3  
 Banerjee, D., O’Shea, E., Doyle, J. G., & Goossens, M. 2001, *A&A*, 371, 1137  
 De Pontieu, B., Erdélyi, R., & De Moortel, I. 2005, *ApJ*, 624, L61  
 Dymova, M. V., & Ruderman, M. S. 2007, *A&A*, 463, 759  
 Erdélyi, R., & Verth, G. 2007, *A&A*, 462, 743  
 Gonzales, R. C., & Woods, R. E. 1992, *Digital Image Processing* (Reading: Addison-Wesley)  
 Ireland, J., Walsh, R. W., Harrison, R. A., & Priest, E. R. 1999, *A&A*, 347, 355  
 Jess, D. B., Andic, A., Mathioudakis, M., Bloomfield, D. S., & Keenan, F. P. 2007, *A&A*, 473, 943  
 Marsh, M. S., & Walsh, R. W. 2006, *ApJ*, 643, 540  
 Mathioudakis, M., Seiradakis, J. H., Williams, D. R., Avgoloupis, S., Bloomfield, D. S., & McAteer, R. T. J. 2003, *A&A*, 403, 1101  
 McAteer, R. T. J., Gallagher, P. T., Bloomfield, D. S., Williams, D. R., Mathioudakis, M., & Keenan, F. P. 2004, *ApJ*, 602, 436  
 McAteer, R. T. J., Young, C. A., Ireland, J., & Gallagher, P. T. 2007, *ApJ*, 662, 691  
 Muzy, J. F., Bacry, E., & Arneodo, A. 1993, *Phys. Rev. E*, 47, 875  
 Nakariakov, V. M., Ofman, L., Deluca, E. E., Roberts, B., & Davila, J. M. 1999, *Science*, 285, 862  
 Nakariakov, V. M., & Verwichte, E. 2005, *Living Rev. Sol. Phys.*, 2, 3  
 O’Shea, E., Banerjee, D., & Doyle, J. G. 2006, *A&A*, 452, 1059  
 ———. 2007, *A&A*, 463, 713  
 O’Shea, E., et al. 2001, *A&A*, 368, 1095  
 Ritz, W. 1908, *J. Reine Angew. Math.*, 135, 1  
 Ruderman, M. S. 2005, in *Proc. 11th European Solar Physics Meeting*, ed. D. Danesy et al. (ESA SP-600; Noordwijk: ESA), 96  
 Schrijver, C. J., Aschwanden, M. J., & Title, A. M. 2002, *Sol. Phys.*, 206, 69  
 Terradas, J., Oliver, R., & Ballester, J. L. 2006, *ApJ*, 650, L91  
 Torrence, C., & Compo, G. P. 1998, *Bull. Amer. Meteor. Soc.*, 79, 61  
 Verth, G., van Doorsselaere, T., Erdélyi, R., & Goossens, M. 2007, *A&A*, 475, 341  
 Verwichte, E., Nakariakov, V. M., Ofman, L., & DeLuca, E. E. 2004, *Sol. Phys.*, 223, 77  
 Wang, T. J., & Solanki, S. K. 2004, *A&A*, 421, L33